

Impurity effects in twisted carbon nanotubes

Yuriy G. Pogorelov*

IFIMUP, Departamento de Física, Universidade do Porto, Porto, Portugal,

Volodymyr Turkowski†

Department of Physics, University of Central Florida, FL 32816, USA

Vadim M. Loktev‡

N.N. Bogolyubov Institute for Theoretical Physics, NAS of Ukraine, Kyiv, Ukraine,

(Dated: December 31, 2024)

We consider electronic spectra of twisted carbon nanotubes and their perturbation by impurity atoms absorbed at different positions on nanotube surface within the framework of Anderson hybrid model. A special attention is given to the cases when 1D Weyl (massless Dirac) modes are present in the nanotube spectrum and their hybridization with localized impurity states produces, with growing impurity concentration c , onset of a mobility gap near the impurity level and then opening, at yet higher c , of some narrow range of delocalized states within this mobility gap. Such behaviors are compared with similar effects in the previously studied 2D graphene, carbon nanoribbons, and non-twisted carbon nanotubes. Some possible practical applications are discussed.

PACS numbers:

I. INTRODUCTION

Carbon nanotubes (CNT's) [1–6] are a broad class of 1D-like structures formed on the base of 2D graphene [7–9], with an important possibility for their electronic spectra to include 1D Weyl modes (WM's) [3]. This importance is due to the combination of linear low-energy dispersion of charge carriers with their 1D density of states, giving promises for very sensitive controls over conductive, optical and other physical properties of these systems.

In analogy with known conductivity tuning in semiconductors, such controls can be realized by introduction of impurities (dopants) but specifics of CNT's is in variety of their dimensional and topological parameters that can qualitatively change the phase structure of low energy eigenstates and their response to external factors. These issues are broadly discussed for 1D carbon nanoribbons (CNR's) and for two basic CNT classes: zigzag nanotubes (ZNT's) and armchair nanotubes (ANT's). But there is a much wider general field of CNT structures between these two limits, known as twisted nanotubes (TNT's) [1, 2], especially rich in their topological parameters and opening new ways to control their conducting behaviors.

Various technological methods for TNT synthesis are now in active development [11–14], also their electronic structure is being studied theoretically, including the first principles approaches [15].

The main purpose of the present work is the theoretical description of electronic dynamics in various TNT's, dif-

fering by their dimension (diameter) and topology (twisting angle), and in establishing the conditions for their maximum sensitivity to dopants and to external controls.

The following presentation begins from definition of lattice structure parameters in TNT's (Sec. II), then continued by the analysis of their electronic spectra in the tight-binding approximation with special emphasis on the DLM's parameters (Sec. III). The most important study of impurity effects on WM's is done in the T-matrix approximation (Sec. IV) and then completed by its validity justification (Sec. V). The final discussion of the obtained results and their possible practical applications is given in Sec. VI. Some supplementary materials are presented in Appendices A, B, C.

II. GEOMETRY OF TWISTED NANOTUBES

Each carbon nanotube (CNT) can be obtained by rolling of a carbon nanoribbon (CNR) cut out from the graphene plane so that its edges will seamlessly match at rolling. Usually, CNR's are classified by their edges, the simplest types being a zigzag nanoribbon (ZNR), with its edges along the graphene basic vector \mathbf{a}_1 , and an armchair nanoribbon (ANR), with those along the graphene unit cell diagonal $\mathbf{a}_1 + \mathbf{a}_2$ (with the lattice constant $|\mathbf{a}_1| = |\mathbf{a}_2| = a \approx 2.46\text{\AA}$). But CNT's (having no edges) are classified by the normals to their axes, thus an ANR gets rolled into a zigzag nanotube (ZNT) and a ZNR does into an armchair nanotube (ANT).

More generally, any CNR (and the related CNT) can be labeled by two natural numbers n and m that define the basis vectors of its rectangular unit cell, the chiral (transversal) vector:

$$\mathbf{C}_h = \frac{n\mathbf{a}_1 + m\mathbf{a}_2}{g}, \quad (1)$$

*Electronic address: ypogorel@fc.up.pt

†Electronic address: Volodymyr.Turkowski@ucf.edu

‡Electronic address: vloktev@bitp.kyiv.ua

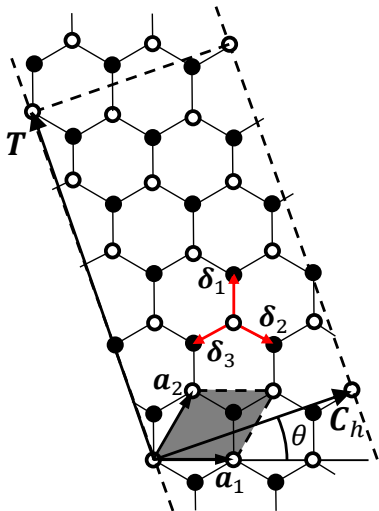


FIG. 1: The (2,1) TNT unfolded unit cell based on the vectors $\mathbf{C}_h = 2\mathbf{a}_1 + \mathbf{a}_2$ and $\mathbf{T} = -4\mathbf{a}_1 + 5\mathbf{a}_2$ and the graphene unit cell (shadowed) based on vectors \mathbf{a}_1 and \mathbf{a}_2 with two atomic sites (white and black circles). The nearest-neighbor vectors δ_ν (red) and the chiral angle θ are indicated.

and the translational (longitudinal) vector:

$$\mathbf{T} = \frac{(2n+m)\mathbf{a}_2 - (2m+n)\mathbf{a}_1}{g'}, \quad (2)$$

where g is the greatest common divisor of n, m and g' is that of $2n+m, 2m+n$. The total number of atoms in the unit cell:

$$M = \frac{4C_h T}{\sqrt{3}a^2} = 4 \frac{n^2 + mn + m^2}{gg'}, \quad (3)$$

is always even (by equivalency of two graphene sublattices) and the CNT full length is considered much longer of its translational period T . Also, without loss of generality, we take $n \geq m$ in what follows.

One limiting CNT type is ZNT ($m = 0, g = g' = n$) with the chiral period $C_h = a$ (along the circumference $C_h g = na$) and the translational period $T = \sqrt{3}a$. Another limit is ANT ($n = m, g = n, g' = 3n$) with the chiral period $C_h = \sqrt{3}a$ (along the circumference $C_h g = \sqrt{3}na$) and the translational period $T = a$.

All other n, m choices refer to TNT's with the periods C_h and T by Eqs. 1, 2. Each TNT can be also defined by its diameter $D = C_h g / \pi$ and chiral angle:

$$\theta = \arctan \frac{\sqrt{3}m}{2n+m}, \quad (4)$$

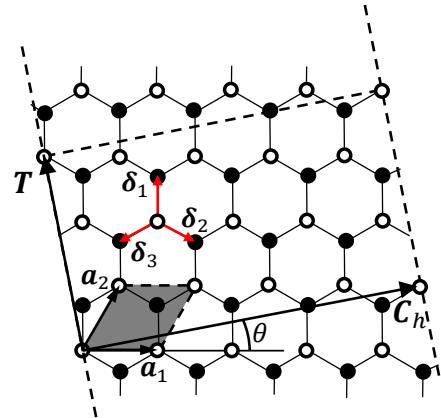


FIG. 2: The (4,1) TNT unfolded unit cell based on the vectors $\mathbf{C}_h = 4\mathbf{a}_1 + \mathbf{a}_2$ and $\mathbf{T} = -2\mathbf{a}_1 + 3\mathbf{a}_2$ differs from that of the (2,1) one by its smaller chiral angle θ while the total numbers of atoms in both cases are the same:

$$M = 28.$$

between the \mathbf{C}_h and \mathbf{a}_1 vectors, with its values $0 < \theta < \pi/6$ (the ZNT and ANT limits). Some TNT examples are presented by their unfolded unit cells in Figs. 1, 2. Each unit cell can be labeled by two indices: p for its translational period, and j for its chiral period, and yet each atomic site in this cell can be labeled by its s index.

III. ELECTRONIC TYPES OF TWISTED NANOTUBES

Physically, two basic CNT electronic types can be denoted:

- * insulating, presenting a finite energy gap around the Fermi level and

- * metallic, with their spectrum including pairs of 1D WM's crossed at zero-energy Fermi level. Our next consideration is focused on the latter ones.

It is known that any metallic CNT structure should satisfy the basic condition [3]:

$$\frac{n-m}{g} = 3l \quad (5)$$

with a whole l number, and its simplest realizations are readily found in all ANT's and in $(3l, 0)$ ZNT's. For a

much wider range of TNT's, these conditions are analyzed in what follows.

To begin with, the local Fermi operators $a_{p,j,s}$ for all s sites ($1 \leq s \leq M$) in the p, j unit cell are combined into the local M -spinor:

$$a_{p,j} = \begin{pmatrix} a_{p,j,1} \\ a_{p,j,2} \\ \dots \\ a_{p,j,M} \end{pmatrix}. \quad (6)$$

Then the TNT translational invariance with the C_h, T periods by Eqs. 1, 2 suggests, in similarity to the previously analyzed ZNT and ANT cases, the Fourier expansion of this spinor components in quasi-continuous translational momenta $-\pi < k < \pi$ and in transversal wave numbers $0 \leq q \leq g-1$:

$$a_{p,j,s} = \frac{1}{2\pi\sqrt{M}} \int_{-\pi}^{\pi} \sum_{q=0}^{g-1} dk \exp[i(kt_{p,j,s} + 2\pi qc_{j,s})] \alpha_{k,q,s}, \quad (7)$$

where $t_{p,j,s}$ and $c_{j,s}$ are respectively longitudinal (in T units) and chiral (in C_h units) coordinates of the p, j, s -position. Alike that by Eq. 6 for local operators, the $\alpha_{k,q,s}$ wave operators can be also combined into the wave M -spinor $\alpha_{k,q}$.

The following treatment of TNT electronic dynamics is done in the approximation of nearest neighbor hopping between carbon sp^2 orbitals with the same constant parameter $\gamma \approx 2.8$ eV as in 2D graphene [8], equivalent to the zone-folding approximation [16] (see on its plausibility below in Sec. VI). In this approximation, the TNT Hamiltonian is written in terms of wave spinors as:

$$H = \gamma \sum_{k,q} \alpha_{k,q}^\dagger \hat{H}(k,q) \alpha_{k,q}. \quad (8)$$

Here the $M \times M$ Hermitian matrix $\hat{H}(k,q)$ has only three non-zero elements in each of its rows and columns, of the form $z_\nu(k,q) = e^{i\varphi_\nu(k,q)}$, $\nu = 1, 2, 3$ (or their complex conjugates $z_\nu^*(k,q)$). Their phases:

$$\begin{aligned} \varphi_1(k,q) &= \frac{a}{\sqrt{3}}(k \cos \theta - \frac{2\pi q}{C_h} \sin \theta), \\ \varphi_2(k,q) &= -\frac{a}{\sqrt{3}}[k \sin(\frac{\pi}{6} + \theta) - \frac{2\pi q}{C_h} \cos(\frac{\pi}{6} + \theta)], \\ \varphi_3(k,q) &= -\varphi_1(k,q) - \varphi_2(k,q), \end{aligned} \quad (9)$$

result from the k, q -Fourier transformed products of local operators at nearest-neighbor sites separated by the corresponding vectors $\delta_{1,2,3}$ (see Fig. 1), so their equilibrium: $\sum_\nu \varphi_\nu(k,q) = 0$, follows from the evident equilibrium: $\sum_\nu \delta_\nu = 0$, of these vectors.

The particular positions of each $z_\nu(k,q)$ element in this $M \times M$ matrix depend on the way to enumerate all the $M \gg 1$ atomic sites in the TNT unit cell, generating a huge variety of possible matrix configurations.

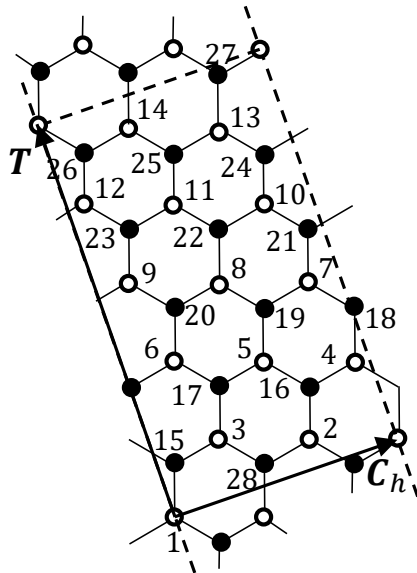


FIG. 3: Numeration of atoms within the (2,1) TNT unit cell by Fig. 1, in the order of two sublattices, each in the order of their t -coordinates.

Some their unification can be reached with the following sublattice-separated numeration way:

- * the first $M/2$ numbers attributed to atoms from the first sublattice in the increasing order of their t coordinates,

- * the next $M/2$ numbers follow in the same order for their nearest neighbors from the second sublattice (e.g., at δ_1 separation, as in the examples by Figs. 3, 4).

This brings the Hamiltonian matrix to a more suitable blockwise form:

$$\hat{H}(k,q) = \begin{pmatrix} 0 & \hat{h}(k,q) \\ \hat{h}^\dagger(k,q) & 0 \end{pmatrix}, \quad (10)$$

where the $\hat{h}(k,q)$ block of $M/2$ dimension and its Hermitian conjugated $\hat{h}^\dagger(k,q)$ describe the hoppings between two sublattices.

Thus, the site numbering as for the (2,1) TNT in Fig. 3 leads to a 14×14 submatrix $\hat{h}(k,q)$ of the multidagonal form explicitly presented by Eq. A2 (Appendix A), while that for (4,1) TNT in Fig. 4 gives it in another multidagonal form as by Eq. A1, with their $z_j(k,q)$ elements defined from Eq. 9 for each n, m choice.

Generally, the TNT spectrum consists of Mg one-dimensional modes $\varepsilon_{j,k}$ with $1 \leq j \leq Mg$, given by the

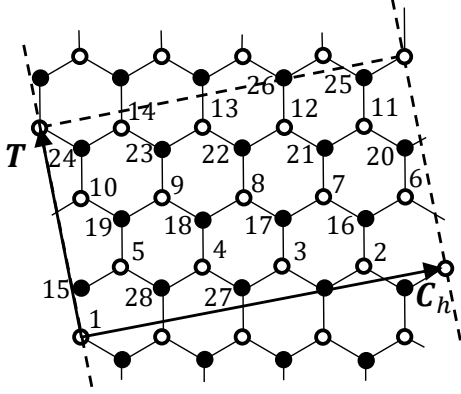


FIG. 4: Numeration, similar to that by Fig. 3, for the (4,1) TNT unit cell by Fig. 2.

roots of secular equation:

$$D(\varepsilon, k, q) = \det \left(\varepsilon \hat{1} - \gamma \hat{H}(k, q) \right) = 0. \quad (11)$$

This determinant is presented as an $M/2$ -degree polynomial of ε^2 :

$$D(\varepsilon, k, q) = \sum_{j=0}^{M/2} (-1)^j D_j(k, q) \gamma^{M-2j} \varepsilon^{2j}, \quad (12)$$

and, for a given q value, its roots define a set of $M/2$ positive eigen-energies and of their $M/2$ negative counterparts (from the total of Mg modes).

It should be noted that, unlike the simpler cases of 2D graphene (2 atomic sites in unit cell) and ZNT's or ANT's (4 atomic sites in unit cell), secular equations for TNT's of $M/2 \geq 14$ orders do not admit general algebraic solutions, thus restricting their treatment to numerical calculations or to certain simplifications near the spectrum special points.

Evidently, all TNT's outside the condition by Eq. 5 are insulating, but even metallic TNT's (satisfying that condition) contain WM's in their spectra only for the single (from the total of g) transversal wave number $q = 0$ in the Fourier series by Eq. 7, when the phases by Eq. 9 get simplified to:

$$\begin{aligned} \varphi_1(k, 0) &= 2 \frac{m+2l}{M} ak, & \varphi_2(k, 0) &= -2 \frac{m+l}{M} ak, \\ \varphi_3(k, 0) &= -\frac{2l}{M} ak. \end{aligned} \quad (13)$$

It can be readily seen that WM presence in any CNT spectrum implies the equation for zeroth order coefficient from Eq. 12:

$$D_0(k, 0) = 0, \quad (14)$$

and each its root in k defines a Dirac point crossed by two WM's. So Eq. 14 permits quantitative detection of Dirac points in the TNT spectrum.

Alternatively, these points follow from a simpler equation:

$$\sum_{\nu=1}^3 z_{\nu}(k, 0) = 0. \quad (15)$$

It relates to the fact that a zero eigenvalue of $\hat{H}(k, 0)$ implies zero eigenvalue of the submatrix $\hat{h}(k, 0)$, obtained from the $M/2$ -vector equation:

$$\sum_{j'=1}^{M/2} h_{j,j'}(k, 0) \psi_{j'}(k) = 0, \quad (16)$$

for the relative $M/2$ -eigenvector $\psi(k)$ of $\hat{h}(k, 0)$. Summing all the components of this vector equation gives:

$$\sum_{j=1}^{M/2} \sum_{j'=1}^{M/2} h_{j,j'}(k, 0) \psi_{j'}(k) = 0. \quad (17)$$

Then the multidagonal structure of $\hat{h}(k, 0)$ brings it to the factored form:

$$\sum_{\nu=1}^3 z_{\nu}(k, 0) \sum_{j=1}^{M/2} \psi_j(k) = 0, \quad (18)$$

whose solutions should formally come from zeros of each factor. Supposing this factor to be the first sum, as given by Eq. 15, one finds Eq. 16 to hold for every its component only with the eigenvector $\psi_j(k) = \text{const}$ (for all j from a given sublattice), which assures the second sum to be nonzero. Contrariwise, if $\sum_i \psi_j(k) = 0$ is supposed, then Eq. 16 never can hold for every its component, thus suggesting Eq. 15 as the simplest check for WM presence.

These conditions in some TNT's are illustrated by the plot of their multiple 1D BZ's along the relative base vectors $\tilde{\mathbf{T}} = 2\pi\mathbf{T}/T^2$, superposed on 2D graphene multiple BZ's (Fig. 5). It shows that, under the condition by Eq. 5, the 1D BZ line crosses just one K and one K' points from the 2D BZ's at $1/3$ and $2/3$ of its length $M/2$ (in $\tilde{\mathbf{T}}$ units).

Thus at the "1/3" crossing, $k = \pi M/3a$, we get the phases:

$$\begin{aligned} \varphi_1 &= \frac{2\pi}{3}(m+2l), & \varphi_2 &= -\frac{2\pi}{3}(m+l), \\ \varphi_3 &= -\frac{2\pi}{3}l, \end{aligned} \quad (19)$$

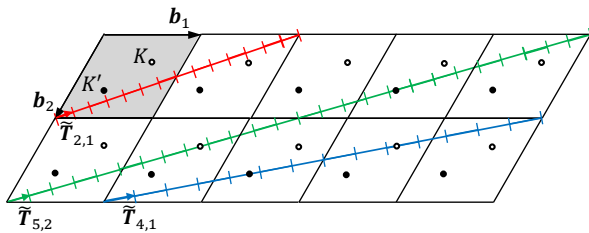


FIG. 5: 2D graphene BZ (shaded) with the Dirac points K (white circle) and K' (black circle) together with its multiple replicas. At their overlapping with $M/2 = 14$ multiples of 1D BZ for metallic (4,1) TNT (blue) or with $M/2 = 26$ such multiples for metallic (5,2) TNT (green), each line passes through two Dirac points (white and black circles), but those are never met by the line of $M/2 = 14$ multiples for insulating (2,1) TNT (red).

so the resulting z_ν values are defined by the three integers $u_1 = (m + 2l) \pmod{3}$, $u_2 = (m + l) \pmod{3}$, and $u_3 = l \pmod{3}$. For any whole l and for any permitted $m \pmod{3} \neq 0$, the (u_1, u_2, u_3) triple is a certain permutation of $(0, 1, 2)$, assuring the condition by Eq. 15. Evidently, the same triples take place for the "2/3" crossing.

In more detail, the calculated polynomial coefficients in Eq. 12 for the case of (4,1) TNT are given explicitly in Appendix B. Then the straightforward calculation of Eq. 14 using the form of Eq. B1 confirms its two roots, $k = \pm 2\pi/3$ as Dirac points (each achieved within a proper multiple of 1D BZ), resulting in 4 WM's within the total of 28 modes, as seen from the complete numerical solution of secular Eq. 11 in Fig. 6.

The resting 24 modes occupy the energy range outside the Dirac window of width Δ_{DW} around the Fermi level, also shown in Fig. 6. Within this window, the full TNT spectrum can be restricted to only its four WM's.

This can be compared to the case of (2,1) TNT (with no WM's expected), here the secular determinant at $q = 0$ again takes the form of Eq. 12 but with different coefficients, also presented in Appendix B. The same check by Eq. 14 for (2,1) TNT with use of Eq. B2 readily shows that here $D_0(k, 0)$ never turns zero along the whole k range, thus excluding WM's in this TNT spectrum as seen also from its complete numerical solution in Fig. 7.

The following treatment of low-energy electronic spectra and impurity effects on them is focused on WM's with their two practical parameters: the Fermi density of states $\rho_F = 4/M\gamma$ and the Fermi velocity $v_F = (\gamma/\hbar)\partial\varepsilon_{k,1}/\partial k|_{k=K}$ (in $\gamma/(hT)$ units). Together, they define the parameter of locator, $G_0 = \rho_F T/(2\hbar v_F)$ (decisive for the local impurity level broadening). For non-

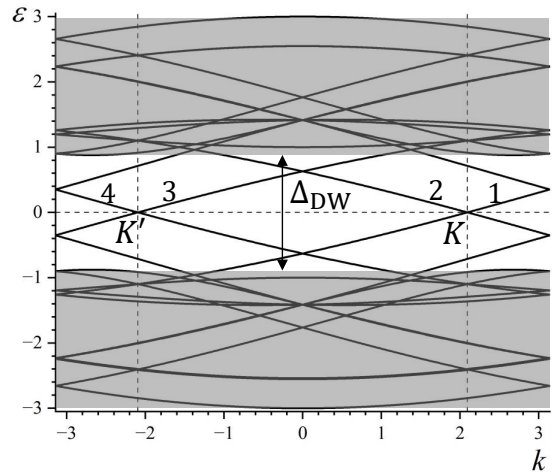


FIG. 6: The set of 28 energy bands for (4,1) TNT vs longitudinal momentum k (in the $1/T$ scale) at transversal number $q = 0$ includes 4 WM's (numbered 1, 2, 3, 4) crossed at Dirac points K and K' (vertical dashed lines). The ranges of resting 24 bands outside the Dirac window Δ_{DW} are shaded.

twisted nanotubes, this parameter is known to decrease with growing their diameter D , as $G_0 = 4a/(\pi D\gamma)$ for ZNT and as $G_0 = a/(2\pi D\gamma)$ for ANT [31].

The Fermi velocity in a given TNT can be found analytically from the first two terms in the series by Eq. 12:

$$v_F = \frac{\gamma}{\hbar} \sqrt{\frac{\partial^2 D_0(k, 0)/\partial k^2}{2D_1(k, 0)}} \Big|_{k=K}. \quad (20)$$

Thus, for the case of (4,1) TNT with $T = \sqrt{7}a$, $\rho_F = 1/7$, and the functions $D_0(k, 0)$, $D_1(k, 0)$ given by Eq. B1, the result by Eq. 20 (in $\gamma T/\hbar$ units) reproduces exactly the standard graphene value $\sqrt{3}/2$ (in $\gamma a/(\hbar)$ units). Then the locator G_0 value for this TNT of diameter $D \approx 1.459a$ results ≈ 0.082 , lower of that for the wider (3,3) ANT of $D \approx 1.654a$.

When going to TNT's of yet higher (n, m) dimensions, obtaining of full analytical expressions for their secular determinants, like Eq. B1, turns already difficult for available calculation sources. But an easier estimate for v_F is obtained from the direct secular equation:

$$\gamma \sum_{j'} h_{j,j'}(k, 0) \psi_{j'}(k) = \varepsilon_{1,k} \psi_j(k), \quad (21)$$

(with the band index 1 for the WM as in Fig. 6) by expanding the non-zero elements $z_\nu(k, 0)$ of the $\hat{h}(k, 0)$ matrix near the Dirac point K up to linear terms in $\kappa = k - K$, approximating the eigenvector components by their constant value: $\psi_j(k) \approx \psi_j(K) = \text{const}$, and taking the WM eigen-energy as $\varepsilon_{1,k} \approx \hbar v_F \kappa$. Then the

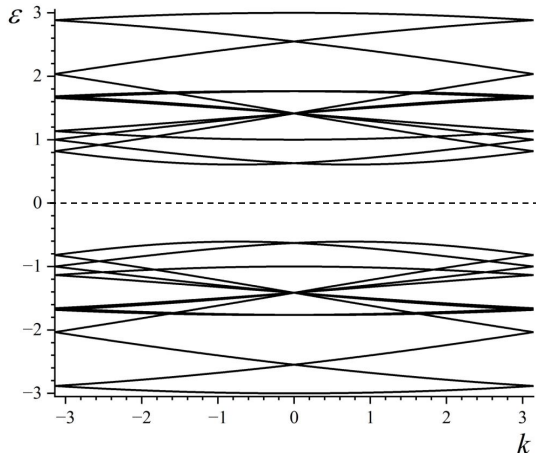


FIG. 7: The set of 28 energy bands for (2, 1) TNT *vs* k at $q = 0$ does not include WM's.

Fermi velocity follows as:

$$v_F = \frac{\gamma}{\hbar} \left| \sum_{\nu=1}^3 \frac{dz_{\nu}(k, 0)}{dk} \right|_{k=K}, \quad (22)$$

which can be readily calculated with use of Eq. 13 for any TNT satisfying the Eq. 5 condition. The simple and important result of this calculation (see its details in Appendix C) is that v_F (in $\gamma T/\hbar$ units) stays always equal $\sqrt{3}/2$.

This result permits to express locator through TNT diameter as:

$$G_0 = \frac{\sqrt{3}a^2}{\gamma(\pi D)^2}, \quad (23)$$

that means a qualitatively faster G_0 decrease with D than the above indicated $G_0 \propto 1/D$ for simple ZNT's and ANT's. The physical reason for this is the proportional growth of both TNT periods: $C_h = \sqrt{3}T = \pi D$ (under the Eq. 5 condition), to give $M = 4C_h T/\sqrt{3} = (2\pi D)^2/3$, in contrast to the only growth of transversal period $C_h = \pi D$ at fixed longitudinal period $T = a$ in ZNT's or $T = \sqrt{3}a$ in ANT's.

So, the next example of (5,2) TNT with its periods $C_h = \sqrt{39}a$, $T = \sqrt{13}a$ and the total of $M = 52$ modes (Fig. 8) also satisfies Eq. 15 for $k = \pm 2\pi/3$ and presents 4 WM's that give a lower $\rho_F = 1/13$. For this TNT of diameter $D \approx 1.99a$ the value of locator $G_0 \approx 0.044$ is already below of that for the wider (6,6) ANT ($D \approx 3.308a$). One more example is the (7, 1) TNT with its

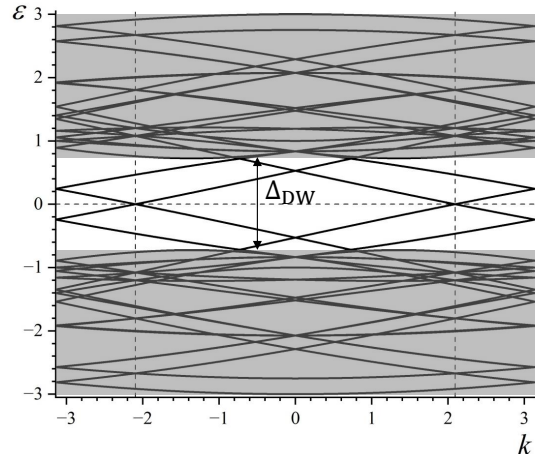


FIG. 8: The set of 52 energy bands for (5, 2) TNT *vs* k at $q = 0$.

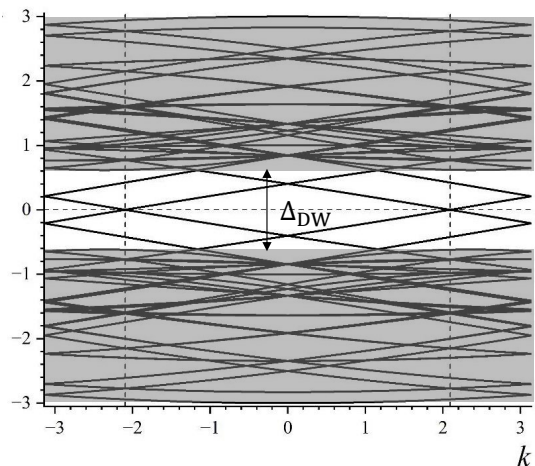


FIG. 9: The set of 76 energy bands for (7, 1) TNT *vs* k at $q = 0$. Both sets include 4 WM's crossed at $k = \pm 2\pi/3$ (vertical dashed lines).

periods $C_h = \sqrt{57}a$, $T = \sqrt{19}a$ and with $M = 76$ modes (Fig. 9). Its diameter $D \approx 2.402a$ used in Eq. 23 gives the locator value as low as $G_0 \approx 0.0305$ and this TNT overcomes in its sensitivity the (9,9) ANT, as wide as of $D \approx 4.96a$.

A resume of these estimates presented in Table I and in Fig. 10 shows progressive advantages of properly chosen TNT's *vs* simple ZNT's and ANT's (of comparable width) in sensitivity of their WM's to low-energy impurity levels.

Now we are in a position to consider perturbations of low-energy electronic spectra in such TNT's under disor-

System	D (a units)	G_0 ($1/\gamma$ units)
ZNT(6,0)	1.91	2/3
ZNT(12,0)	3.82	1/3
ANT(3,3)	1.654	$1/(6\sqrt{3})$
ANT(6,6)	3.308	$1/(12\sqrt{3})$
ANT(9,9)	4.96	$1/(18\sqrt{3})$
TNT (4,1)	1.459	$1/(7\sqrt{3})$
TNT (5,2)	1.988	$1/(13\sqrt{3})$
TNT (7,1)	2.404	$1/(19\sqrt{3})$
TNT (7,4)	3.07	$1/(31\sqrt{3})$
TNT (8,5)	3.62	$1/(43\sqrt{3})$

TABLE I: Comparison of WM parameters for different ZNT's and ANT's with those for TNT's.

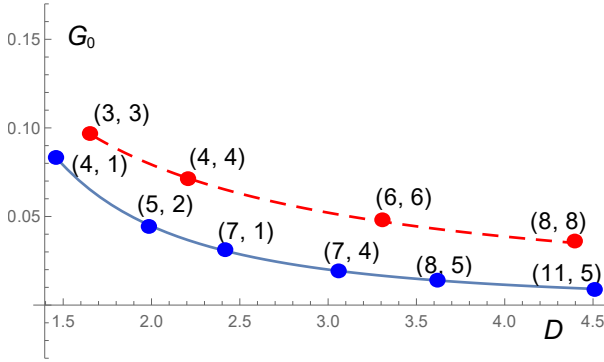


FIG. 10: Variation of the locator parameter G_0 with the nanotube diameter D for different ANT (red) and TNT (blue) types.

der from impurity centers.

IV. IMPURITY EFFECTS ON WM'S IN TWISTED NANOTUBES

Various disorder effects on carbon nanosystems are being studied both experimentally [17–19] and theoretically [20–27]. In particular, important effects on their electronic spectra are expected from d -metal (Cu, Ag, Au) impurity adatoms [28–30] and for the case of TNT's they can be treated in a similar way to the previous analysis in simpler ANT's and ZNT's [31]. First of all, we reduce the TNT spectrum to its four WM's with the mode indices as in Fig. 3 and combine them into the 4-spinor:

$$\Psi_k = \begin{pmatrix} \alpha_{k,1} \\ \alpha_{k,2} \\ \alpha_{k,3} \\ \alpha_{k,4} \end{pmatrix} \quad (24)$$

Then the WM-reduced TNT Hamiltonian is written

as:

$$H_{WM} = \sum_k \Psi_k^\dagger \hat{h}_k \Psi_k, \quad (25)$$

where the 4×4 matrix:

$$\hat{h}_k = \begin{pmatrix} \varepsilon_{k,K} \hat{\tau}_3 & 0 \\ 0 & \varepsilon_{k,K'} \hat{\tau}_3 \end{pmatrix}, \quad (26)$$

includes 2×2 Pauli $\hat{\tau}_3$ matrices. In accordance with the result from Eq. 22, the eigenenergies can be linearized near two Dirac points as:

$$\varepsilon_{k,K} \approx \frac{\sqrt{3}}{2} \left(k - \frac{2\pi}{3} \right), \quad \varepsilon_{k,K'} \approx \frac{\sqrt{3}}{2} \left(k + \frac{2\pi}{3} \right).$$

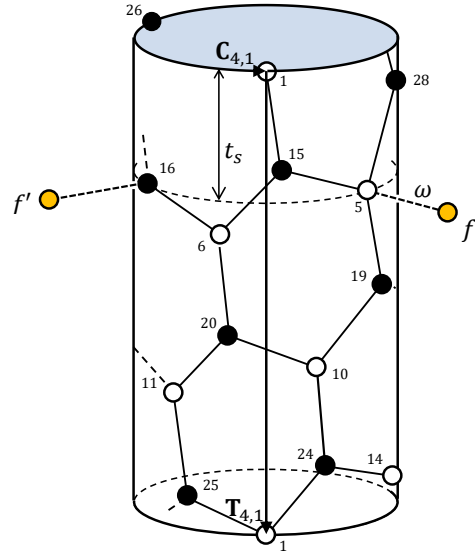


FIG. 11: The cylindrical unit cell of the (4,1) TNT with atoms numeration as in Fig. 4. The impurity adatoms (yellow circles) are linked through the hybridization constant γ to the underlying TNT sites. Note the coincidence of longitudinal coordinates, $t_f = t_{f'}$, for the sites $f = 5$ and $f' = 16$ (from different sublattices).

For impurity adatoms located over random TNT sites f , we apply the Anderson s - d hybrid model [32] with its two perturbation parameters: impurity (low-energy) level ε_{res} and the constant ω of (weak) hybridization with

the nearest carbon atoms (Fig. 11). As was shown by the previous studies, this two-parametric model turns more adequate to the considered situation than simpler one-parametric ones, as random on-site energy shift Anderson model [33] or Lifshitz model of fixed energy shift on random sites [34].

Within the framework of Anderson hybrid model, the perturbation Hamiltonian is written in terms of the impurity local operators β_f and the Ψ_k spinors as:

$$H' = \sum_f \left[\varepsilon_0 \beta_f^\dagger \beta_f + \left(\frac{\omega}{\sqrt{N}} \sum_k e^{ikt_f} \beta_f^\dagger u_f^\dagger \Psi_k + \text{h.c.} \right) \right], \quad (27)$$

where t_f is the f site longitudinal coordinate and the row spinors $u_f^\dagger = \pm(i, i, i, i)/\sqrt{M}$ relate to the eigen-vectors of WM's with $k = K, K'$ at f site (see after Eq. 18).

The next treatment is done as usually in terms of two-time (advanced) Green functions (GF's), Fourier transformed in energy [35–37]:

$$\langle\langle A|B \rangle\rangle_\varepsilon = \frac{i}{\pi} \int_{-\infty}^0 e^{i(\varepsilon-i0)t} \langle\{A(t), B(0)\}\rangle dt, \quad (28)$$

including the Heisenberg representation operators $O(t) = e^{iHt} O e^{-iHt}$ with the Hamiltonian H , their grand-canonical statistical average $\langle O(t) \rangle = \text{Tr} [e^{-\beta(H-\mu)} O(t)] / \text{Tr} [e^{-\beta(H-\mu)}]$ with inverse temperature β and chemical potential μ , and the anti-commutator $\{.,.\}$ of fermion operators. These GF's are calculated from the equation of motion:

$$\varepsilon \langle\langle A|B \rangle\rangle_\varepsilon = \langle\{A(0), B(0)\}\rangle + \langle\langle [A, H]|B \rangle\rangle_\varepsilon, \quad (29)$$

with the commutator $[.,.]$. In what follows the energy sub-index at GF's is mostly omitted (or enters directly as its argument).

Consider the GF matrix $\hat{G}_{k,k'} = \langle\langle \Psi_k | \Psi_{k'}^\dagger \rangle\rangle$, here Eq. 29 with the Hamiltonian $H = H_{WM} + H'$ takes the form:

$$\hat{G}_{k,k'} = \hat{G}_k^{(0)} \delta_{k,k'} + \frac{\omega}{\sqrt{N}} \sum_f e^{-ikt_f} \hat{G}_k^{(0)} \langle\langle \beta_f | \Psi_{k'}^\dagger \rangle\rangle u_f, \quad (30)$$

with the unperturbed GF matrix $\hat{G}_k^{(0)} = (\varepsilon - \hat{h}_k)^{-1}$ and the Kronecker δ -symbol. Now continue the chain of equations, separating at each next step the terms with GF's already present at previous steps. Thus, for the mixed GF in the r.h.s. of Eq. 30 we obtain:

$$\begin{aligned} \langle\langle \beta_f | \Psi_{k'}^\dagger \rangle\rangle (\varepsilon - \varepsilon_{res}) &= \frac{\omega}{\sqrt{N}} e^{ik't_f} u_f^\dagger \hat{G}_{k',k'} \\ &+ \frac{\omega}{\sqrt{N}} \sum_{k'' \neq k'} e^{ik''t_f} u_f^\dagger \hat{G}_{k'',k'}, \end{aligned} \quad (31)$$

separating the most important momentum-diagonal $\hat{G}_{k',k'}$ term. Then for the resting GF's we obtain:

$$\hat{G}_{k'',k'} = \frac{\omega}{\sqrt{N}} \sum_{f'} e^{-ik''t_{f'}} \hat{G}_{k''}^{(0)} \langle\langle \beta_{s'} | \Psi_{k'}^\dagger \rangle\rangle u_{f'}. \quad (32)$$

Here the term with $f' = f$ in the r.h.s. generates in Eq. 31 the impurity self-energy factor $\Sigma_0 = \omega^2 G_0$ with the locator function:

$$G_0 = \frac{1}{N} \sum_k u_f^\dagger \hat{G}_k^{(0)} u_f \quad (33)$$

(in what follows considered at $\varepsilon = 0$) beside the mixed GF. Then Eq. 31 is rewritten as:

$$\begin{aligned} \langle\langle \beta_f | \Psi_{k'}^\dagger \rangle\rangle (\varepsilon - \tilde{\varepsilon}_{res}) &= \frac{\omega}{\sqrt{N}} e^{ik't_f} u_f^\dagger \hat{G}_{k',k'} \\ &+ \frac{\omega}{\sqrt{N}} \sum_{k'' \neq k'} e^{ik''t_f} u_f^\dagger \hat{G}_{k'',k'}, \end{aligned} \quad (34)$$

with the renormalized resonance term $\tilde{\varepsilon}_{res} = \varepsilon_{res} + \Sigma_0$. Now mixed GF's can be eliminated from Eq. 30 to present it as GF scattering by the effective impurity potential:

$$\begin{aligned} \hat{G}_{k,k'} &= \hat{G}_k^{(0)} \delta_{k,k'} \\ &+ \frac{1}{N} \sum_{k'',f} e^{i(k''-k)t_f} \hat{G}_k^{(0)} \frac{\omega^2}{\varepsilon - \tilde{\varepsilon}_{res}} u_f^\dagger \hat{G}_{k'',k'} u_f. \end{aligned} \quad (35)$$

Separation of the $k'' = k'$ term from this sum gives:

$$\begin{aligned} \hat{G}_{k,k'} &= \hat{G}_k^{(0)} \left[\delta_{k,k'} + \frac{\omega^2}{\varepsilon - \tilde{\varepsilon}_{res}} u_f^\dagger \hat{G}_{k',k'} u_f \right. \\ &\left. + \frac{1}{N} \sum_{k'' \neq k',f} e^{i(k''-k)t_f} \frac{\omega^2}{\varepsilon - \tilde{\varepsilon}_{res}} u_f^\dagger \hat{G}_{k'',k'} u_f \right], \end{aligned} \quad (36)$$

and its next iterations restricted to only scatterings on the same impurity site s result in the T-matrix solution for the momentum-diagonal GF [38]:

$$\left(\hat{G}_{k,k} \right)^{-1} = \left(\hat{G}_k^{(0)} \right)^{-1} - c \hat{T}, \quad (37)$$

with the (scalar in this case) T-matrix:

$$\hat{T} = \frac{\omega^2}{\varepsilon - \tilde{\varepsilon}_{res}} \hat{1}. \quad (38)$$

Within the adopted perturbation model, each TNT specifics enters this solution only through the value of locator G_0 in the renormalized impurity resonance $\tilde{\varepsilon}_{res}$.

Now, in full analogy with the previous study on impurity induced DLM spectrum restructuring in simple ANT's and ZNT's [31], we can conclude about this in different TNT's just from the data by Table I.

Generally, such restructuring with growing impurity concentration c results from the competition between

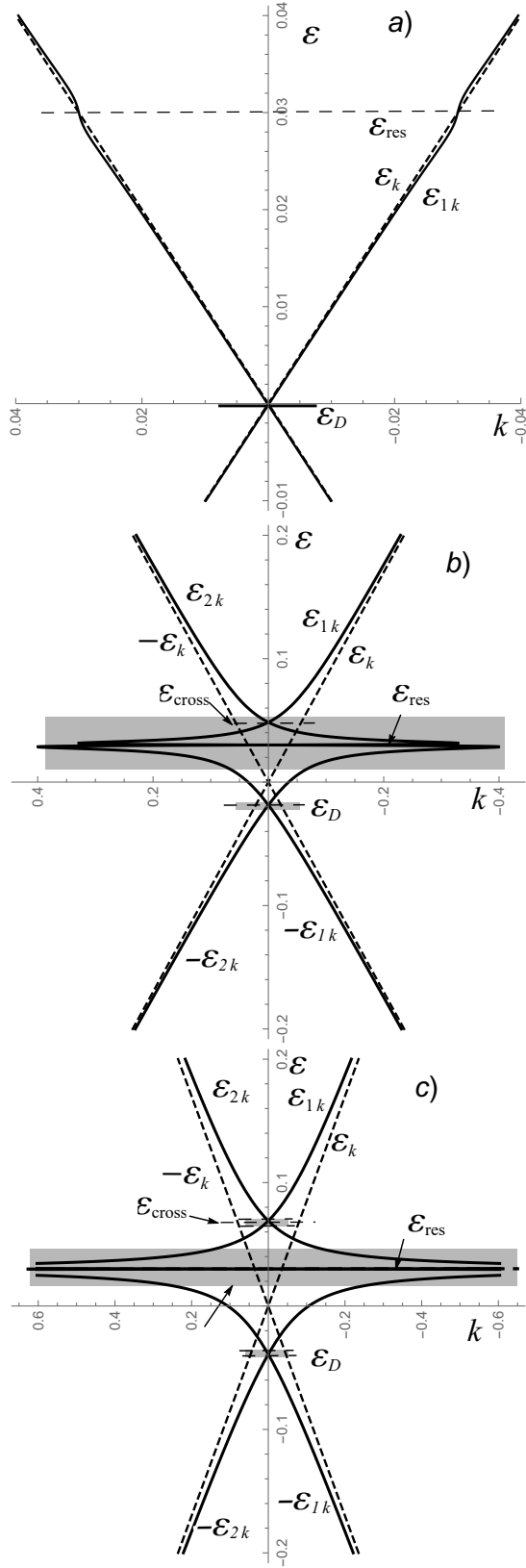


FIG. 12: Restructuring of the (7,1) TNT spectrum with growing Cu impurity concentration c . a) At lowest $c \ll c_0 \approx 4 \cdot 10^{-4}$, WM's are only slightly modified near the impurity level $\varepsilon_{res} = 0.03$. b) At higher $c_0 < c < c_1 = 0.0304$, a stronger WM's modification with onset of a mobility gap (shaded) occurs around ε_{res} . c) At yet higher $c > c_1$, this mobility gap is split by a narrow conducting range (with velocity $\ll v_F$) between the separate ε_{res} and ε_{cross} mobility gaps. Another mobility gap near the shifted Dirac level ε_D

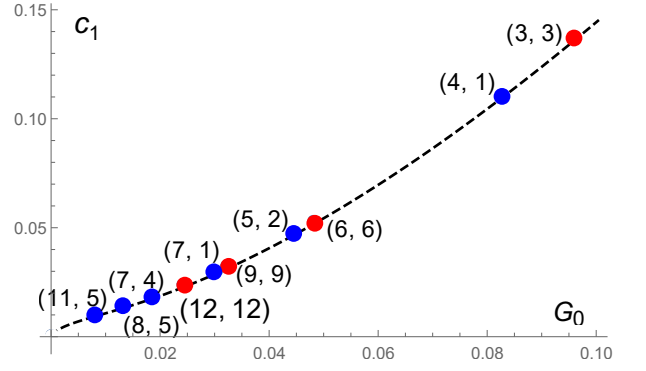


FIG. 13: Critical concentrations c_1 for different carbon nanostructures along their G_0 parameter by Eq. 40.

The TNT's (blue circles) realize the lowest critical values compared to 2D graphene (green) and to much wider ANR's (brown) and ANT's (red).

growing quasiparticle wavelength and its shortening mean free path, expressed by the Ioffe-Regel criterion [39] and leading to the onset of Mott's mobility edges ε_{mob} [40] between conducting and localized ranges in the spectrum. For doped CNT's, the outcomes of this competition are defined by two critical values [27], the lower one:

$$c_0 = \frac{|\omega G_0|^2}{2} \sqrt{1 + 4 \frac{\varepsilon_{res}}{\gamma^2 |G_0|}}, \quad (39)$$

for the emergence of a range of localized states (mobility gap) around the impurity resonance energy ε_{res} (Fig. 12b), and the higher one,

$$c_1 \approx \sqrt{0.01|G_0| + 20|G_0|^3}, \quad (40)$$

for the resonance splitting of this mobility gap to open a novel narrow delocalized range between two mobility edges: above ε_{res} and below the WM's crossing point ε_{cross} (Fig. 12c).

Then the diagram of such c_1 values in function of the G_0 parameter, previously obtained for ZNT's, ANT's [31], and also for some carbon nanoribbons [27], can be completed with the present data for properly chosen TNT's. As seen from Fig. 13, the latter ones appear as the most promising objects for important electronic phase transitions in such quasi-1D carbon nanostructures at lowest impurity concentrations.

It can be yet noted that the properly chosen TNT's, besides a faster decay of their locator with growing diameter, $G_0 \propto 1/D^2$ by Eq. 23, against $G_0 \propto 1/D$ in ZNT's and ANT's, also present a slower decay of their Dirac window in the energy spectrum, numerically approximated as $\Delta_{DW} \propto 1/D^{3/4}$, against $\Delta_{DW} \propto 1/D$ in ZNT's and ANT's, both these behaviors being favorable for TNT's practical applications.

V. BEYOND T-MATRIX

We can yet briefly discuss the extension of the T-matrix approximation by Eq. 37 to the more general self-energy form:

$$(\hat{G}_k)^{-1} = (\hat{G}_k^0)^{-1} - \hat{\Sigma}_k, \quad (41)$$

with the self-energy matrix $\hat{\Sigma}_k$ presented by the group expansion (GE) [38]:

$$\hat{\Sigma}_k = c\hat{T}(\hat{1} + c\hat{B}_k + \dots). \quad (42)$$

Here the sum:

$$\hat{B}_k = \sum_r (e^{-ikt} \hat{A}_t + \hat{A}_t^2) (\hat{1} - \hat{A}_t^2)^{-1} \quad (43)$$

describes the effect of multiple scatterings by a pair of impurities at longitudinal distance t between them through the related scattering matrix $\hat{A}_t = \hat{T}G_t$. Notably, the correlator function $G_t = (4M)^{-1} \sum_{k' \neq k} e^{ik't} u^\dagger \hat{G}_{k'}^{(0)} u$ extends the above discussed locator function G_0 to a finite distance t (with the important possibility for zero distance $t = 0$ to be included into the sum in Eq. 43, see Fig. 11). The omitted terms in the r.h.s. of Eq. 42 correspond to contributions by clusters of three and more impurities.

However, by analogy with the previous study on disordered ZNT's and ANT's [31], the GE corrections to the above T-matrix result for disordered TNT's are negligible (beyond a very narrow vicinity of ε_{res} deeply within the localized range) and thus do not change the general composition of their spectra. Also these simple T-matrix results are found in a good agreement with their another extension to the self-consistent form [41].

VI. DISCUSSION AND CONCLUSIONS

The given analysis demonstrates either similarities and differences of impurity disorder effects on WM's in various types of carbon nanotubes, to contribute into the general context of conductance in 1D-like disordered systems [42–44]. It indicates importance of each nanotube topology (besides only its size) for the detailed electronic structure, especially at low energies. The known earlier qualitative difference between metallic CNT's (with strong restructuring of their WM's under low impurity doping) and insulating ones (practically insensitive to such doping) is yet added with a progressive advantage of metallic TNT's against metallic ZNT's and ANT's in their sensitivity to dopants (at growing their diameter).

In this context, yet the validity of the adopted approximation by Eq. 8 can be discussed. As seen from the known analysis on metallic and insulating ZNT's and ANT's [45], the first principles corrections to the simple zone-folding results can modify the initially gapped spectra (but far from the Dirac points), however they

have practically no effect on zero-gap WM's, like those of our central interest here, so justifying (at least, qualitatively) the above conclusions about impurity effects on their spectra.

Under these effects, the most important factors of TNT effectiveness are the extremely fine intervals between conducting and localized energy ranges (as shown in the example by Fig. 12) and also the Fermi level position getting fixed close to ε_{res} at all $c > c_0$ [27, 31], which then permits at $c > c_1$ repeated insulator/metal and metal/insulator transitions at *continuous* variation of external control (within a few mV scale). Also, there can be various types of these controls (electric and magnetic fields, e.m. radiation, etc.) used in such high sensitivity devices with properly chosen TNT elements.

Possible practical applications of doped TNT's electronic properties can be sought first of all in the field of controlled conductance devices, analogs to the traditional semiconducting diodes and their derivatives but with qualitatively higher levels of sensitivity and compactness. Otherwise, they can also provide new perspectives for high density memory elements [46, 47], chemical/organic sensing elements [48], (infrared) radiation receivers and transformers, supercapacitors, and many others.

VII. ACKNOWLEDGEMENTS

The authors are grateful to V.P. Gusynin, A.A. Eremko and S.G. Sharapov for a substantial discussion of different aspects of the present work. The work of VT was supported in part by United States Department of Energy under Grant No DE-FG02-07ER46354, VML acknowledges the support from Grant ID 1290587 of the Simons Foundation (USA).

Appendix A: TNT matrices

Using the position numbering as for the (4, 1) TNT in Fig. 4 leads to a 14×14 submatrix \hat{h} of the multi-diagonal

form (with the k, q arguments omitted for brevity):

$$\hat{h} = \begin{pmatrix} z_1 & 0 & 0 & 0 & 0 & 0 & 0 & 0 & 0 & 0 & z_2 & z_3 & 0 & 0 & 0 \\ 0 & z_1 & 0 & 0 & 0 & 0 & 0 & 0 & 0 & 0 & 0 & z_2 & z_3 & 0 & 0 \\ 0 & 0 & z_1 & 0 & 0 & 0 & 0 & 0 & 0 & 0 & 0 & 0 & z_2 & z_3 & 0 \\ 0 & 0 & 0 & z_1 & 0 & 0 & 0 & 0 & 0 & 0 & 0 & 0 & 0 & z_2 & z_3 \\ z_3 & 0 & 0 & 0 & z_1 & 0 & 0 & 0 & 0 & 0 & 0 & 0 & 0 & 0 & z_2 \\ z_2 & z_3 & 0 & 0 & 0 & z_1 & 0 & 0 & 0 & 0 & 0 & 0 & 0 & 0 & 0 \\ 0 & z_2 & z_3 & 0 & 0 & 0 & z_1 & 0 & 0 & 0 & 0 & 0 & 0 & 0 & 0 \\ 0 & 0 & z_2 & z_3 & 0 & 0 & 0 & z_1 & 0 & 0 & 0 & 0 & 0 & 0 & 0 \\ 0 & 0 & 0 & z_2 & z_3 & 0 & 0 & 0 & z_1 & 0 & 0 & 0 & 0 & 0 & 0 \\ 0 & 0 & 0 & 0 & z_2 & z_3 & 0 & 0 & 0 & z_1 & 0 & 0 & 0 & 0 & 0 \\ 0 & 0 & 0 & 0 & 0 & z_2 & z_3 & 0 & 0 & 0 & z_1 & 0 & 0 & 0 & 0 \\ 0 & 0 & 0 & 0 & 0 & 0 & z_2 & z_3 & 0 & 0 & 0 & z_1 & 0 & 0 & 0 \\ 0 & 0 & 0 & 0 & 0 & 0 & 0 & z_2 & z_3 & 0 & 0 & 0 & z_1 & 0 & 0 \\ 0 & 0 & 0 & 0 & 0 & 0 & 0 & 0 & z_2 & z_3 & 0 & 0 & 0 & z_1 & 0 \end{pmatrix}, \quad (\text{A1})$$

where $z_1 = e^{i3k/14}$, $z_2 = e^{-ik/7}$, $z_3 = e^{-ik/14}$ (with k in $1/T$ units).

Otherwise, using the numbering for (2, 1) TNT as in Fig. 3 gives such submatrix as:

$$\hat{h} = \begin{pmatrix} z_1 & 0 & 0 & 0 & 0 & 0 & 0 & 0 & 0 & 0 & 0 & 0 & z_2 & z_3 & 0 \\ 0 & z_1 & 0 & 0 & 0 & 0 & 0 & 0 & 0 & 0 & 0 & 0 & 0 & z_2 & z_3 \\ z_3 & 0 & z_1 & 0 & 0 & 0 & 0 & 0 & 0 & 0 & 0 & 0 & 0 & 0 & z_2 \\ z_2 & z_3 & 0 & z_1 & 0 & 0 & 0 & 0 & 0 & 0 & 0 & 0 & 0 & 0 & 0 \\ 0 & z_2 & z_3 & 0 & z_1 & 0 & 0 & 0 & 0 & 0 & 0 & 0 & 0 & 0 & 0 \\ 0 & 0 & z_2 & z_3 & 0 & z_1 & 0 & 0 & 0 & 0 & 0 & 0 & 0 & 0 & 0 \\ 0 & 0 & 0 & z_2 & z_3 & 0 & z_1 & 0 & 0 & 0 & 0 & 0 & 0 & 0 & 0 \\ 0 & 0 & 0 & 0 & z_2 & z_3 & 0 & z_1 & 0 & 0 & 0 & 0 & 0 & 0 & 0 \\ 0 & 0 & 0 & 0 & 0 & z_2 & z_3 & 0 & z_1 & 0 & 0 & 0 & 0 & 0 & 0 \\ 0 & 0 & 0 & 0 & 0 & 0 & z_2 & z_3 & 0 & z_1 & 0 & 0 & 0 & 0 & 0 \\ 0 & 0 & 0 & 0 & 0 & 0 & 0 & z_2 & z_3 & 0 & z_1 & 0 & 0 & 0 & 0 \\ 0 & 0 & 0 & 0 & 0 & 0 & 0 & 0 & z_2 & z_3 & 0 & z_1 & 0 & 0 & 0 \\ 0 & 0 & 0 & 0 & 0 & 0 & 0 & 0 & 0 & z_2 & z_3 & 0 & z_1 & 0 & 0 \\ 0 & 0 & 0 & 0 & 0 & 0 & 0 & 0 & 0 & 0 & z_2 & z_3 & 0 & z_1 & 0 \end{pmatrix}. \quad (\text{A2})$$

with $z_1 = e^{i5k/14}$, $z_2 = e^{-i2k/7}$, $z_3 = e^{-ik/14}$.

Appendix B: Secular determinants

The straightforward calculation of secular determinant for (4,1) TNT with use of the matrices \hat{h} by Eq. A1 (and

its conjugated \hat{h}^\dagger) gives the coefficients in Eq. 12 as:

$$\begin{aligned} D_0(k, 0) &= 10892 + 16238 \cos k + 8268 \cos 2k \\ &\quad + 1396 \cos 3k + 72 \cos 4k - 2 \cos 5k, \\ D_1(k, 0) &= 159040 + 163912 \cos k + 45136 \cos 2k \\ &\quad + 4536 \cos 3k + 112 \cos 4k, \\ D_2(k, 0) &= 838614 + 648080 \cos k + 106848 \cos 2k \\ &\quad + 5880 \cos 3k + 42 \cos 4k, \\ D_3(k, 0) &= 2361576 + 1371468 \cos k + 140952 \cos 2k \\ &\quad + 3892 \cos 3k, \\ D_4(k, 0) &= 4130182 + 1767192 \cos k + 111650 \cos 2k \\ &\quad + 1344 \cos 3k, \\ D_5(k, 0) &= 4833192 + 1467452 \cos k + 53592 \cos 2k \\ &\quad + 28 \cos 3k, \\ D_6(k, 0) &= 3938452 + 804776 \cos k + 14980 \cos 2k, \\ D_7(k, 0) &= 2281180 + 20852 \cos k + 2188 \cos 2k, \\ D_8(k, 0) &= 946358 + 68684 \cos k + 126 \cos 2k, \\ D_9(k, 0) &= 280420 + 9996 \cos 2k, \\ D_{10}(k, 0) &= 58548 + 812 \cos k, \\ D_{11}(k, 0) &= 8372 + 28 \cos k, \\ D_{12}(k, 0) &= 777, \quad D_{13}(k, 0) = 42, \\ D_{14}(k, 0) &= 1. \end{aligned} \quad (\text{B1})$$

A similar procedure for (2,1) TNT with use of the matrices by Eq. A2 (having the same dimension) gives another set of coefficients for Eq. 12:

$$\begin{aligned} D_0(k, 0) &= 44884 - 8478 \cos k + 460 \cos 2k - 2 \cos 3k, \\ D_1(k, 0) &= 419104 - 47488 \cos k + 1120 \cos 2k, \\ D_2(k, 0) &= 1702568 - 105056 \cos k + 952 \cos 2k, \\ D_3(k, 0) &= 3998064 - 120512 \cos k + 336 \cos 2k, \\ D_4(k, 0) &= 6087326 - 77000 \cos k + 42 \cos 2k, \\ D_5(k, 0) &= 6380416 - 25984 \cos k, \\ D_6(k, 0) &= 4761064 - 2856 \cos k, \\ D_7(k, 0) &= 2574424 - 872 \cos k, \\ D_8(k, 0) &= 1014860 - 308 \cos k, \\ D_9(k, 0) &= 290388 - 28 \cos 2k, \\ D_{10}(k, 0) &= 59360, \quad D_{11}(k, 0) = 8400, \\ D_{12}(k, 0) &= 777, \quad D_{13}(k, 0) = 42, \\ D_{14}(k, 0) &= 1. \end{aligned} \quad (\text{B2})$$

This difference is completely due to different phases ϕ_j of their matrix elements z_j as indicated after Eqs. A2, A1, resulting from the difference in chiral angles θ for these two TNT's when used in Eq. 9.

Appendix C: Fermi velocity calculation

Let us consider the explicit secular equation for a WM:

$$\gamma \sum_{j'=1}^{M/2} h_{j,j'}(k) \psi_{j'}(k, 0) = \varepsilon_k \psi_j(k, 0). \quad (\text{C1})$$

By the blockwise structure of $\hat{h}(k)$ matrix, the j, j' indices in this equation belong to different sublattices, namely: j to the 1st sublattice and j' to the 2nd sublattice. Also this sum is restricted to only three non-zero matrix elements $z_\nu(k, 0)$, so its expansion up to linear terms in $\kappa = k - K$ (with the account of Eq. 15) reads:

$$\sum_{\nu=1}^3 z_\nu(k, 0) = i \sum_{\nu=1}^3 \left[z_\nu(k, 0) \frac{d\varphi_\nu(k)}{dk} \right]_{k=K} \kappa + O(\kappa^2). \quad (\text{C2})$$

Denoting the constant values $\psi_j(K, 0)$ for two sublattices as ψ_1 and ψ_2 , we get the relation: $\psi_1 = i\psi_2$, and, using them as eigenvector components in Eq. C1, obtain:

$$\varepsilon_k = \gamma \left| \sum_{\nu=1}^3 z_\nu(k, 0) \frac{d\varphi_\nu(k)}{dk} \right|_{k=K} \kappa + O(\kappa^2). \quad (\text{C3})$$

With the derivatives provided by Eq. 13:

$$\begin{aligned} \frac{d\varphi_1(k)}{dk} &= 2a \frac{m+2l}{M}, & \frac{d\varphi_2(k)}{dk} &= -2a \frac{m+l}{M}, \\ \frac{d\varphi_3(k)}{dk} &= -a \frac{2l}{M}, \end{aligned} \quad (\text{C4})$$

the sum in Eq. C3 gives:

$$v_F = \frac{2\gamma a}{\hbar M} |m(z_1 - z_2) + l(2z_1 - z_2 - z_3)|. \quad (\text{C5})$$

Then, using again Eq. 15 and also Eq. 5, we rewrite this as:

$$v_F = \frac{2\gamma a}{\hbar M} |nz_1 - mz_2|, \quad (\text{C6})$$

and, with the relations $|z_1| = |z_2| = 1$, $\text{Re } z_1 z_2 = -\frac{1}{2}$, finally obtain:

$$v_F = \frac{\sqrt{3} \gamma T}{2 \hbar}, \quad (\text{C7})$$

that is the Fermi velocity for any proper TNT (in its $\gamma T/\hbar$ units) reproduces the standard graphene form (in the $\gamma a/\hbar$ units).

-
- [1] S. Iijima, *Physica B* 323, 1 (2002).
 - [2] A.H. Nevidomskyy, G. Csányi, and M.C. Payne, *Phys. Rev. Lett.* 91, 105502 (2003).
 - [3] J-C. Charlier, X. Blase, and S. Roche, *Rev. Mod. Phys.* 79, 677 (2007).
 - [4] K. Wakabayashi, K. Sasaki, T. Nakanishi, and T. Enoki, *Sci. Technol. Adv. Mater.* 11, 054504 (2010).
 - [5] M.F.L. De Volder, S.H. Tawfik, R.H. Baughman, and A.J. Hart, *Science*, 339, 535 (2013).
 - [6] M. Inagaki and F. Kang, *J. Mater. Chim. A* 2, 13193 (2014).
 - [7] S.V. Morozov, K.S. Novoselov, F. Schedin, D. Jiang, A.A. Firsov, and A.K. Geim, *Phys. Rev. B* 72, 201401 (2005).
 - [8] A.H. CastroNeto, F. Guinea, N.M.R. Peres, K.S. Novoselov, and A.K. Geim, *Rev. Mod. Phys.* 81 109 (2009).
 - [9] D. Tománek, *Guide Through the Nanocarbon Jungle*, Morgan & Claypool Publishers (2014).
 - [10] C.L. Kane and E.J. Mele, *Phys. Rev. Lett.* 78, 1932 (1997).
 - [11] E. Muñoz, W.K. Maser, A.M. Benito, G.F. de la Fuente, M.T. Martínez, *Synth Met.* 103, 2490 (1999).
 - [12] H.E. Lim, Y. Miyata, R. Kitaura, Y. Nishimura, Y. Nishimoto, S. Irle, J.H. Warner, H. Kataura, and H. Shinohara, *Nat. Commun.* 4, 2548 (2013).
 - [13] S. Rathinavel, K. Priyadharshini, and D. Panda, *J. Mater. Sci. Eng. B* 268, 115095 (2021).
 - [14] S. Lou, B. Lyu, J. Chen, L. Qiu, S. Ma, P. Shen, Z. Zhang, Y. Xie, Q. Liang, K. Watanabe, T. Taniguchi, F. Ding, and Z. Shi, *Sci. Rep.* 13, 4328 (2023).
 - [15] K. Kato, T. Koretsune, and S. Saito, *J. Phys.: Conf. Ser.*, 302, 012007 (2011).
 - [16] G.G. Samsonidze, R. Saito, A. Jorio, M. A. Pimenta, A. G. Souza Filho, A. Grüneis, G. Dresselhaus, and M.S. Dresselhaus, *J. Nanosci. Nanotechnol.*, 3, 431 (2003).
 - [17] S. Jalili, M. Jafari, and J. Habibian, *J. Iran. Chem. Soc.* 5, 641 (2008).
 - [18] P.T. Araujo, M. Terrones, and M.S. Dresselhaus, *Mater. Today* 15, 98 (2012).
 - [19] J. Vejpravova, B. Pacakova, and M. Kalbac, *Analyst* 141, 2639 (2016).
 - [20] M. Fujita, K. Wakabayashi, K. Nakada, and K. Kusakabe, *J. Phys. Soc. Jpn* 65, 1920 (1996).
 - [21] K. Nakada, M. Fujita, G. Dresselhaus and M.S. Dresselhaus, *Phys. Rev. B* 54, 17954 (1996).
 - [22] T.O. Wehling, M.I. Katsnelson, and A.I. Lichtenstein, *Phys. Rev. B* 80, 085428 (2009).
 - [23] Y.V. Skrypnik and V.M. Loktev, *Low Temp. Phys.* 44, 1112 (2018).
 - [24] S. Irmer, D. Kochan, J. Lee and J. Fabian, *Phys. Rev. B*

- 97, 075417 (2018).
- [25] Y.G. Pogorelov, V.M. Loktev, and D. Kochan, *Phys. Rev. B* 102, 155414 (2020).
- [26] Y.G. Pogorelov, D. Kochan, and V.M. Loktev, *Low Temp. Phys.* 47, 754 (2021).
- [27] Y.G. Pogorelov, and V.M. Loktev, *Phys. Rev. B* 106, 224202 (2022).
- [28] A.H. Castro Neto, V.N. Kotov, J. Nilsson, V.M. Pereira, N.M.R. Peres, B. Uchoa, *Solid State Commun.* 149, 1094 (2009).
- [29] M. Amft, S. Lebégue, O. Eriksson, and N.V. Skorodumova, *J. Phys.: Condens. Matter* 23, 395001 (2011).
- [30] O. Faye, *African Review of Physics* 7:0036:313-318 (2012).
- [31] Y.G. Pogorelov, V.M. Loktev, *Phys. Rev. B* 110, 075142 (2024).
- [32] P.W. Anderson, *Phys. Rev.* 124, 41 (1961).
- [33] P.W. Anderson, *Phys. Rev.* 109, 1492 (1958).
- [34] I.M. Lifshitz, *Adv. Phys.* 13(52), 483 (1964).
- [35] D. Zubarev, *Sov. Phys. Uspekhi* 3, 320 (1960).
- [36] V.L. Bonch-Bruевич and S.V. Tyablikov, *The Green Function Method in Statistical Mechanics*, North Holland Publishing House (1962).
- [37] E.N. Economou, *Green's Functions in Quantum Physics*, Springer (1979).
- [38] M.A. Ivanov, V.M. Loktev, and Y.G. Pogorelov, *Phys. Reports* 153, 209 (1987).
- [39] A.F. Ioffe and A.R. Regel, *Progress Semicond.* 2, 237 (1960).
- [40] N.F. Mott, *Phil. Mag.* 102, 835 (1962).
- [41] K.F. Freed, *Phys. Rev. B* 5, 4802 (1972).
- [42] T. Ando and T. Nakanishi, *J. Phys. Soc. Jpn* 67, 1704 (1998).
- [43] T. Ando, *Semicond. Sci. Technol.* 15, R13 (2000).
- [44] R. Vosk, D. A. Huse, and E. Altman, *Phys. Rev. X* 5, 0310332 (2015).
- [45] R. Barnett, E. Demler and E. Kaxiras, *Phys. Rev. B* 71, 035429 (2005).
- [46] E.C. Ahn, H.-S.P. Wong, and E. Pop, *Nat. Rev. Mater.* 3(3), 18009 (2018).
- [47] F. Yang, Z. Liu, X. Ding, Y. Li, C. Wang, and G. Shen, *Chip* 3, 2, 100086 (2024).
- [48] M. Pumera, A. Ambrosia, E.L.K. Chnga, and H.L. Poh, *Chem. Sci.* 3, 3347 (2012).